Ceramics International 50 (2024) 15124–15133

Contents lists available at ScienceDirect

Ceramics International

journal homepage: www.elsevier.com/locate/ceramint

Microstructural evolution and electrochemical corrosion characteristics of Ti–Ni matrix composite in NaCl and HCl solutions

Oluwasegun Eso Falodun [a,*], Samuel Ranti Oke [a], Moses M. Solomon [b], Abiodun Bayode [a]

[a] Department of Mechanical Engineering, North-West University, Potchefstroom, South Africa
[b] Department of Chemical and Environmental Engineering, University of Nottingham Ningbo China, Ningbo, China

ARTICLE INFO

Handling Editor: Dr P. Vincenzini

Keywords:
Microstructure
Potentiodynamic polarization
Electrochemical impedance
NaCl
Hydrochloric acid

ABSTRACT

Ti–Ni matrix composites were produced using spark plasma sintering (SPS), a powder metallurgy technique. The influence of Ni-xTiB_2 additions on the titanium matrix microstructure, hardness, and electrochemical properties was investigated. Scanning electron microscopy, hardness analysis incorporating regression analysis, potentiodynamic polarization, and electrochemical impedance spectroscopy tests were used to characterize the titanium matrix composites. The titanium matrix induced microstructural changes, leading to the coexistence of α and β phases along grain boundaries. A more substantial equiaxed α phase was observed in the Ti+5Ni+20TiB_2 composite. The X-ray diffraction analysis showed that the crystal structures of the composites were altered and that the grains were refined. The microhardness increased with the TiB_2 content. The potentiodynamic polarization analysis indicated that the corrosion resistance of the composites improved with the addition of Ni and TiB_2, with the Ti+5Ni+20TiB_2 composite exhibiting the highest corrosion resistance. The electrochemical impedance spectroscopy revealed that the Ti+5Ni+20TiB_2 composite had enhanced diffusion properties and a stable passive layer, further confirming its exceptional corrosion resistance. Additionally, the composites exhibited a distinct capacitive behavior, indicative of strong corrosion resistance. This is characterized by phase angle values close to −90° and high impedance values (10^9 Ω cm^2) at low and medium frequencies. This is due to the formation of a very stable film on the composites in the test solutions (NaCl and HCl).

1. Introduction

Titanium and its alloys have exceptional physical characteristics and properties, including high strength-to-weight ratio, good ductility, biocompatibility, and corrosion resistance. These materials are extensively utilized in numerous industries including aerospace, petrochemical, military, and automotive [1,2]. Titanium alloys are highly resistant to corrosion in many corrosive environments, especially those that oxidize or contain chloride ions. This exceptional corrosion resistance is due to the formation of a very stable oxide film on the surface of the alloy [3,4]. Titanium alloys are the preferred materials for biomedical implants. This is primarily because of their non-toxic nature and the formation of a relatively inert passive film [3,5]. Despite their remarkable corrosion resistance, titanium alloys have some limitations. These include lower hardness, poorer wear resistance, and lower oxidation resistance than superalloys and stainless steels. Moreover, titanium alloys degrade at elevated temperatures, limiting their use in industries that require enhanced mechanical properties at high temperatures [6]. Researchers have suggested incorporating ceramic particles into these materials to overcome these limitations of titanium alloys. This incorporation was achieved using various manufacturing techniques such as casting and powder metallurgy, which can effectively address the concerns regarding the physical and mechanical properties of titanium alloys [7–10].

The synergistic incorporation of metallic sintering additives, specifically nickel, into titanium alloys, along with titanium diboride, aims to improve the mechanical properties and sinterability of the alloys. Nickel's strategically dispersed placement at grain interfaces and triple boundaries results in a continuous intergranular phase. This fosters densification through solid-state diffusion [11]. Furthermore, it improves interfacial bonding strength by facilitating enhanced dislocation pinning and promoting grain boundary cohesion [12,13]. Titanium diboride (TiB_2) is a promising ceramic material that can significantly enhance the mechanical and thermal properties of titanium-based composites. Its exceptional hardness, high melting point, chemical inertness, and lightweight characteristics make it a preferred choice in

* Corresponding author.
E-mail address: segzy201@gmail.com (O.E. Falodun).

https://doi.org/10.1016/j.ceramint.2024.01.431
Received 14 December 2023; Received in revised form 28 January 2024; Accepted 31 January 2024
Available online 1 February 2024

various industrial and engineering applications. This is particularly the case in situations where high-temperature and wear resistance are crucial [14]. In addition, it is generally corrosion-resistant, although its performance in specific corrosive environments depends on various factors. These include temperature, concentration of corrosive agents, and exposure time. In extremely aggressive environments, some corrosion may still occur over time. Nevertheless, TiB_2 is much more resistant than many other materials.

Powder metallurgy (PM) uses compaction and sintering techniques to shape metal powders into components. It is a cost-efficient way of manufacturing titanium components with enhanced mechanical properties and corrosion resistance [15,16]. Spark plasma sintering (SPS) is a state-of-the-art powder metallurgy technique that has emerged as a more efficient alternative to conventional sintering methods [17]. This technique can foster a rapid solidification of alloy powders, to attain full density through the application of pulsed direct current and pressure. SPS offers numerous advantages over conventional sintering methods. The advantages include precise control over sintering parameters such as holding time, cooling time, sintering temperature, heating rate, and sintering pressure. This ensures the optimization of the sintering process and the production of components with reduced porosity and outstanding mechanical properties [18–20]. Also, SPS enables the high-precision creation of intricate components, giving users greater control over the final product [21,22]. SPS technology is now the preferred method for fabricating titanium matrix composites, because of its superior sintering efficiency and exceptional performance. Manufacturing titanium-based composites through an in-situ approach results in a substantial improvement in mechanical properties, due to the formation of ceramic phases at the interfaces. These phases exhibit favorable binding and wettability within the titanium matrix, contributing to enhanced performance [21,23]. In metal-matrix composites (MMCs) reinforced with ceramic particles, the diameter and aspect ratio of these particles significantly influence material behavior. Large ceramic particles (>10 μm) act as stress concentrators under tensile loading, due to their sharp edges and local stiffness mismatch with the matrix. This leads to premature matrix cracking around the particles, ultimately causing MMCs' failure. Thus, optimizing the mechanical performance of MMCs requires the reduction of the size of ceramic particles to sub-micrometer and even nanometer scales. This leads to improved strength, ductility, and fatigue resistance in the MMCs [24,25].

Dong et al. [26] conducted a study investigating the impact of sintering on the microstructural evolution and mechanical properties of titanium matrix composites reinforced with reduced graphene oxides (rGO) through SPS. The findings indicated that the reaction between the titanium matrix and rGO at elevated sintering temperatures led to a homogeneous distribution of micro/nano-sized titanium carbide (TiC) particles within the rGO/titanium composites. Sabahi Namini and Azadbeh [27] examined the microstructural and mechanical properties of a TiB_2-reinforced titanium matrix composite fabricated via SPS. Their analysis revealed the formation of TiB whiskers because of the interaction between the matrix and TiB_2. However, unreacted TiB_2 particles remained due to incomplete chemical reactions. Also, Sulima et al. [28] studied the corrosion behavior of SPS composites reinforced with titanium diboride (TiB_2). They found that composites sintered at a higher temperature of 1100 °C had better corrosion resistance. Additionally, increasing the sintering time further improved the corrosion resistance of these composites. Abu-Warda et al. [29] investigated the corrosion characteristics of an A6005 aluminium matrix composite alloyed with titanium diboride (TiB_2) nanoparticles. They uncovered that the samples processed via mechanical alloying had slightly better corrosion resistance than the A6005 alloy. This improvement is due to the formation of an Al_2O_3 phase, which helps to form a continuous passive layer. Chang et al. [30] evaluated the corrosion resistance of TiB_2 powder (1, 3, and 5 wt%) incorporated into Ti–8Ta–6Ni alloys via vacuum sintering. They found that TiB_2 was uniformly distributed in the titanium matrix, improving its corrosion resistance. Notably, the 3 wt% TiB_2 specimens had the highest polarization resistance and the lowest polarization corrosion current (6.42×10^{-6} A/cm^{-2}), resulting in the best corrosion resistance. Furthermore, the corrosion current initially decreased as the TiB_2 content increased, but subsequently increased (9.72, 6.42, and 8.21 $\times 10^{-6}$ A/cm^{-2}). Investigations by Sahay et al. [31] and Namini et al. [32] support the claim that TiB_2 has excellent corrosion resistance.

The current study comprehensively examines the microstructural evolution, corrosion resistance, and electrochemical behavior of Ti–5Ni-based composites. The study employs both sodium chloride (NaCl) and hydrochloric acid (HCl) solutions to simulate diverse corrosive environments. This in-depth analysis, facilitated by potentiodynamic polarization and electrochemical impedance spectroscopy (EIS), contributes to a deeper understanding of the material's performance in various corrosive conditions. By utilizing both NaCl and HCl solutions, this study enhances a more comprehensive assessment of the composite's durability and suitability for a broader range of practical applications in diverse corrosive environments.

2. Experimental procedure

2.1. Materials

Pure titanium and nickel powders (average particle size: 25 ± 5 μm, purity: 99.9%), supplied by TLS-Technik, and titanium diboride (TiB_2) reinforcement particles (average particle size: 15 ± 5 μm, purity: 99.6%), provided by Weartech Pty, were utilized as composite materials in this investigation. These powders were introduced into the titanium matrix and subjected to mechanical alloying in a planetary ball mill. The latter operated for 8 h at a speed of 100 revolutions per minute (rpm). The ball mill utilized 10 mm diameter alumina balls with a ball-to-powder weight ratio of 10:1. Subsequently, SPS was performed using HHPD–25 SPS machines by the FCT Systeme, from Germany. The sintering operation occurred under vacuum conditions at 1000°C and 50 MPa pressure for 5 min, employing a heating rate of 100°C per minute.

2.2. Microstructural characterization and XRD analysis

To facilitate a detailed phase and metallographic analysis, the samples were divided into smaller sections. The titanium matrix composite was first polished using various SiC abrasive papers up to 8000 grits. It was subsequently refined with 0.3 and 0.5 μm diamond suspension, before undergoing etching. The etching process utilized Kroll's reagent comprising 2 mL of HF, 3 mL of HNO_3, and 95 mL of H_2O, with an etching duration of 45 s. The microstructure of the sintered composites was analyzed using scanning electron microscopy (JEOL JSM-7600 F model) and energy-dispersive spectrometry (EDS). X-ray diffractometry (Philip PW1710) served to identify the phases present in the composites, and the Xpert software was used to assess the presence of all phases.

2.3. Hardness result and regression analysis

The hardness of the cross-sectional area of the sintered composites was measured using a microhardness Vickers machine (FALCON 500 series) with a load of 200 gf applied for 10 s. Regression analysis, a statistical technique, was used to model and analyze the correlation between the hardness (response variable) and the input parameters. This analysis was performed using the Design Expert software version 13.

2.4. Potentiodynamic polarization test

The samples were submerged in epoxy resin during the electrochemical tests, ensuring an exposed surface area of approximately 20 mm^2 to the solutions. Subsequently, potentiodynamic polarization experiments were undertaken by connecting a Gamry potentiostat to a desktop device. The electrochemical experiments were conducted in a

three-electrode cell containing 250 mL of electrolyte solution. The reference electrode was Ag/AgCl and the counter electrode was made of platinum rod. The working electrode was the titanium matrix composite. For the experiments conducted at room temperature, the titanium matrix composites were immersed in electrolyte solutions of 3.5 wt% NaCl and 1 M HCl and were scanned at 0.2 mV/s.

2.5. Electrochemical impedance spectroscopy

The electrochemical impedance spectroscopy (EIS) tests were performed using a computer-controlled Gamry Potentiostat/Galvanostat/ZRA Reference 600 connected to a computer. In these experiments, the working electrode was the titanium matrix composite sample, the reference electrode was an Ag/AgCl electrode (3 M KCl), and the counter electrode was a platinum rod. The open circuit potential was monitored for 30 min before analyzing the impedance characteristics of the working electrode. Subsequently, the EIS measurements were conducted in potentiostatic mode, applying an alternating current signal with an amplitude of 10 mV across a frequency range from 100,000 Hz–0.1 Hz. The obtained electrochemical impedance data were analyzed using the Echem analyst software. To ensure the reproducibility of the results, both polarization and EIS tests were performed in triplicate.

3. Results and discussion

3.1. Microstructural characterization

Fig. 1(a) shows a consistent dispersion of nickel and titanium diboride particles on the titanium powder surface. The particles exhibit slight deformation and uneven shapes, suggesting strong metallurgical bonding. Scattered agglomerates, likely formed through cold welding during mixing [33,34], and large flake-like particles due to severe plastic deformation are also present. These agglomerations could potentially lead to bonding issues at the interface. Therefore, the efficacy of the powder blending method is crucial in achieving homogeneous dispersion [35], as demonstrated by the SEM–EDX analysis in Fig. 1(b). This analysis confirms the effective incorporation of nickel-titanium diboride particles into the titanium matrix. The microstructural characteristics of the titanium alloy, along with the incorporation of reinforced ceramics into the alloy, are depicted in Fig. 1(c–d). In this figure, the microstructure is characterized by a uniform equiaxed grain pattern primarily composed of α-Titanium (α-Ti) phases arranged in a lamellar structure. Notably, there is no evidence of grain enlargement or elongation. This outcome can be attributed to the pinning effect [36]. At a temperature of 1000°C, the introduction of nickel (Ni) into the sintering process has a significant impact on the β transus temperature. This results in the formation of a stable β-titanium phase. This influence derives from nickel's inherent property as a β-phase stabilizing element. The rapid cooling inherent in the sintering procedure impedes the full transformation of β-Ti into α-Titanium (α-Ti). This leads to the coexistence of laminar α and β phases along grain boundaries. This phenomenon results from the interfacial reaction between the reinforcement and matrix powders during the sintering process, culminating in the creation of intermetallic (Ti_2Ni) eutectoid phases [37].

It is of utmost importance to underscore that nickel (Ni) atoms exhibit a greater tendency for diffusion, in comparison to titanium (Ti) atoms. Thus, the vacancies generated tend to aggregate near interfaces or dislocations [38]. Consequently, as illustrated in Fig. 1(b), the microstructure gradually evolves toward an equiaxed grain formation. This follows the introduction of reinforcement into the titanium alloy. The lack of consistent solidification homogeneity initiates a solid-state interaction between TiB_2 and Ti powders, leading to a more even distribution of TiB precipitates. This process preserves the prior β grain boundaries, with minimal incorporation of TiB [39]. Nonetheless, the increased volume percentage of TiB within Ti + Ni+20TiB_2 is linked to a greater volume percentage of the equiaxed α phase. These findings emphasize the impact of TiB precipitates on the morphology of the α phase [39]. Furthermore, the inclusion of nickel also contributes to the refinement of the alloy's microstructure, resulting in enhanced corrosion resistance.

3.2. X-ray diffraction analysis

The X-ray diffraction (XRD) patterns for titanium matrix composites

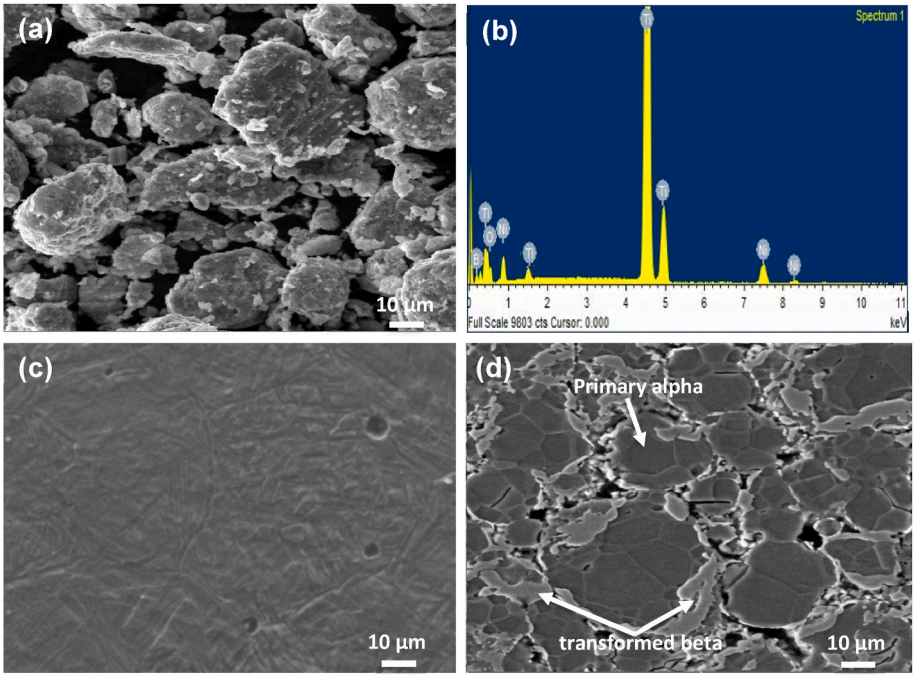

Fig. 1. Scanning electron microscope (SEM) micrographs of composite materials: (a) Mixed titanium-based composite powder, (b) EDX analysis, (c) sintered pure titanium, and (d) sintered Ti–Ni–20TiB_2 composite.

containing 20TiB_2 are presented in Fig. 2. The XRD patterns exhibited a more noticeable intensity peak broadening and a shift toward lower 2θ angles, in comparison to pure titanium. This broadening of intensity peaks indicates the existence of fine grains in both the α and β phases of the titanium composite material. This characteristic implies an increase in residual stress levels and changes in the lattice parameters within the titanium matrix composites. Generally, these residual stresses are due to the temperature variations caused by the rapid heating and cooling cycles occurring during the sintering process. The ensuing modified crystal structures account for the broader peaks. Furthermore, the shift in intensity peak positions signifies a unique crystallographic orientation within the composites. Chao et al. [40] investigated the reinforcement of titanium matrix composite with ZrO_2 particulate. Their findings revealed that the peaks exhibited an increased width and that they shifted towards the left. This observation suggests a modification in the crystal lattice structure. The most significant observation was the widening of XRD peaks, confirming grain refinement within the composites. Grain refinement, associated with numerous smaller crystalline structures, is influenced by lattice strain and crystallite size [41].

3.3. Hardness and regression analysis

The hardness values for the specimens are as follows: Ti (238 ± 2 $HV_{0.2}$), Ti+5Ni (325 ± 5 $HV_{0.2}$), and 5–20% TiB_2 (397 ± 3, 469 ± 6, 510 ± 12, and 592 ± 9 $HV_{0.2}$ respectively). The findings indicate a direct correlation between the ceramic particle (TiB_2) content and the increasing hardness of the titanium matrix in the composite. The hardness increases because the ceramic additives are very hard. Furthermore, the presence of ceramic particles (TiB_2) acts as an effective impediment to the dislocation movement. This constitutes a strong barrier against permanent material deformation [42]. The uniform dispersion of these strengthening phases within the material and the increased number of grain boundaries significantly hampers the dislocation slip. This plays a crucial role in the observed enhancement of microhardness in the titanium matrix composite [14].

The regression analysis for hardness was established by utilizing experimental data with Design Expert Software version 13. The equation of this established model assesses the interactions between the input (reinforcement vol%) and response parameters (hardness), providing insights into the characteristics of the output parameters through the utilization of Design Expert Software. This equation can be expressed as follows:

Let A = Hardness (1)

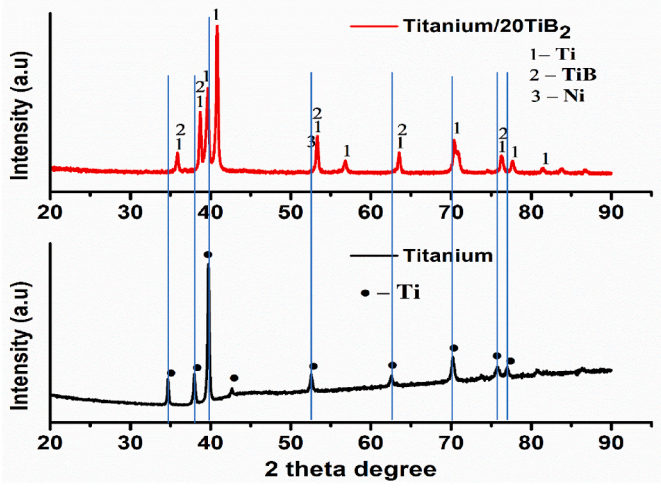

Fig. 2. XRD pattern of sintered titanium and reinforced titanium matrix composite.

$$\text{Microhardness} = +467.63 + 91.67A - 52.86A^2 + 85.33A^3 \quad (2)$$

Table 1 illustrates the ANOVA table about the hardness model, which serves as the basis for qns. (1) and (2). The F-value, as indicated at 6515.76, signifies the model's significance. This significant F-value indicates that there is only a 0.91% chance that such a substantial F-value could be attributed to random noise.

The regression analysis suggests the most feasible model, which is indicated using bold text in Table 2. Specifically, the cubic model is highlighted as the preferred choice among the other models listed. The summary of the Hardness Response model reveals a close match between the predicted R^2, standing at 0.9923, and the adjusted R^2, which is impressively high at 0.9998. This alignment is evident as the difference between these two values falls well below 0.2. This indicates that the model effectively clarifies the connection between the input variables and the hardness response. The p-values below 0.0500 indicate the significance of model terms [43].

3.4. Potentiodynamic polarization of the composite

Fig. 3 illustrates the potentiodynamic polarization curves of the titanium matrix composite immersed in a 3.5 wt% NaCl solution at room temperature. From Fig. 3(a–b), it is evident that all samples display various passive regions. Table 3 shows that pure titanium exhibits a moderate corrosion tendency with an E_{corr} of –336.00 mV/Ag/AgCl, and a corresponding corrosion rate (110.30 mpy × 10^{-3}). However, when nickel (Ni) is added (Ti+5Ni), although the corrosion potential (E_{corr}) drops to –274.00 mV/Ag/AgCl, the corrosion rate significantly decreases to 40.04 mpy × 10^{-3}. This suggests that the presence of nickel improves the corrosion resistance of the material. Interestingly, a further addition of 5 % TiB_2 to Ti+5Ni (Ti+5Ni+5TiB_2) results in an even lower corrosion rate (39.07 mpy × 10^{-3}) despite a relatively low E_{corr} of –191.00 mV/Ag/AgCl. This indicates that the incorporation of TiB_2 nanoparticles enhances the material's corrosion resistance [44]. The Tafel slopes (β_c and β_a) provide insights into the corrosion kinetics of these materials. In the case of Pure Ti, the cathodic and anodic Tafel slopes are 148.10 mV dec^{-1} and –655.50 mV dec^{-1}, respectively. This suggests a significant difference in the rates of reduction and oxidation reactions during corrosion. In contrast, the Ti+5Ni alloy exhibits narrower Tafel slopes (–843.30 mV dec^{-1} for cathodic and 782.60 mV dec^{-1} for anodic), indicating more balanced kinetics. The addition of TiB_2 (Ti+5Ni+5TiB_2) further influences the Tafel slopes, potentially altering the corrosion mechanisms.

The Ti+5Ni+20TiB_2 sample demonstrates a wider active passivation behavior, compared to the other samples. In general, the greater the difference in potential, the higher the titanium matrix's capacity to withstand corrosion [45]. Thus, a lower corrosion current density signifies excellent anti-corrosion characteristics [46]. Therefore, the Ti+5Ni+20TiB_2 sample demonstrated a wider range of passivation compared to the other composites, when exposed to a 3.5 wt% NaCl solution. Furthermore, as shown in Table 3, the Ti+5Ni+20TiB_2 composite exhibits the lowest i_{corr} value (4.15 mpy × 10^{-3}). This indicates an active surface that readily undergoes passivation or slow dissolution, thus demonstrating a highly corrosion-resistant material [47]. This

Table 1
Analysis of variance (ANOVA) table for the hardness model.

Source	Sum of Squares	df	Mean Square	F-value	p-value	
Model	71487.14	3	23829.05	6515.76	0.0091	significant
A-A	2326.92	1	2326.92	636.27	0.0252	
A^2	2444.64	1	2444.64	668.46	0.0246	
A^3	1638.40	1	1638.40	448.00	0.0301	
Residual	3.66	1	3.66			
Cor Total	71490.80	4				

Table 2
Response model summary.

Source	Std. Dev.	R^2	Adjusted R^2	Predicted R^2	PRESS	
Linear	36.91	0.9428	0.9238	0.7884	15128.51	
Quadratic	28.65	0.9770	0.9541	0.6024	28424.76	
Cubic	**1.91**	**0.9999**	**0.9998**	**0.9923**	**551.11**	**Suggested**
Quartic					*	
Fifth					*	Aliased

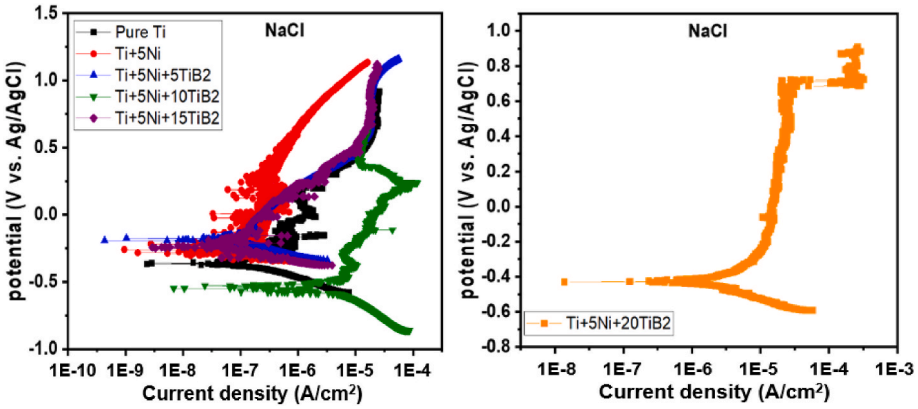

Fig. 3. Potentiodynamic polarization plot of titanium matrix composite in 3.5 wt% NaCl solution.

Table 3
Electrochemical corrosion parameters of sintered Ti and Ti–Ni-xTiB_2 samples following immersion in a 3.5 wt% NaCl solution.

Sample	$-E_{corr}$ (mV/Ag/AgCl)	i_{corr} (nA cm^{-2})	$-\beta_c$ (mV dec^{-1})	β_a (mV dec^{-1})	CR_i (mpy) × 10^{-3}
	NaCl				
Pure Ti	336.00	238.00	148.10	655.50	110.30
Ti+5Ni	274.00	86.30	843.30	782.60	40.04
Ti+5Ni+5TiB2	191.00	84.20	110.50	418.00	39.07
Ti+5Ni+10TiB2	548.00	914.00	100.00	301.40	424.20
Ti+5Ni+15TiB2	244.00	495.00	2099.00	2560.00	229.50
Ti+5Ni+20TiB2	428.00	8.93 μA	375.50	1086.00	4.15

means that the material experiences minimal corrosion and degradation over time when exposed to a corrosive environment. In contrast, Ti+5Ni+10TiB_2, with a corrosion rate of 424.20 mpy × 10^{-3}, shows significantly higher corrosion. This suggests that it is more susceptible to deterioration in a 3.5 wt% NaCl solution.

Moreover, it was observed that the Ti, Ti+5Ni+5TiB_2, Ti+5Ni+10TiB_2, and Ti+5Ni+20TiB_2 samples exhibited a secondary passivation behavior, as illustrated in Fig. 3. Nonetheless, the corrosion potential of Ti+5Ni+10TiB_2 reaches approximately −250 mV/Ag/AgCl, a significant surge occurs in current density. This indicates that Cl^- ions, known for their potent activation ability, infiltrate the passive layer and cause the breakdown of the protective film formed on the surface [48]. As the corrosion potential increases, the secondary passivation behavior leads to the formation of a passive film, reaching a potential of approximately –110 mV/Ag/AgCl. Upon further observation of the Ti+5Ni+20TiB_2 sample, it was noted that the corrosion potential reaches –750 mV/Ag/AgCl, leading to a noticeable shift in the current density. Additionally, a secondary passivation behavior was observed, which concludes at –900 mV/Ag/AgCl. Every sample displayed the development of small corrosion pits on their surfaces, an outcome arising from the combined influences of immersion corrosion and electrochemical corrosion [49]. Considering these corrosion parameters, the corrosion resistance of the six materials follows a descending order as follows: Ti+5Ni+20TiB_2 > Ti+5Ni+5TiB_2 > Ti+5Ni > Ti > Ti+5Ni+15TiB_2 > Ti+5Ni+10TiB_2 in 3.5 wt% NaCl solution as shown in Table 3.

The potentiodynamic polarization curves for the titanium matrix composite when immersed in a 1 M HCl solution. Fig. 4 reveals that each sample exhibits distinct passive regions. An interesting observation is that, as the corrosion potential continues to increase, a sudden shift occurs in the current density across all the samples. This shift indicates the infiltration of Cl^- ions, which possess potent activation capabilities. These cause a rapid disruption of the passive film initially formed on the surface. Generally, a higher E_{corr} value in such cases signifies greater chemical stability and reduced susceptibility to corrosion. Conversely, a smaller i_{corr} value typically indicates a lower corrosion rate and exceptional corrosion resistance [50]. Pure titanium and the Ti+5Ni alloy exhibit different levels of corrosion resistance. Notably, the Ti+5Ni alloy demonstrates superior corrosion resistance, as evidenced by its lower E_{corr} (corrosion potential) of –83.90 mV/Ag/AgCl in comparison to a titanium E_{corr} of –135.00 mV/Ag/AgCl inTable 4. A lower E_{corr} value signifies a higher degree of protection against corrosion. Additionally, the Ti+5Ni alloy showcases a reduced i_{corr} (corrosion current density) of 42.20 nA cm^{-2}. This indicates a slower corrosion rate when compared to titanium's i_{corr} of 57.30 nA cm^{-2}.

Incorporating nickel and titanium diboride (TiB_2) nanoparticles, as seen in Ti+5Ni+5TiB_2 and Ti+5Ni+10TiB_2, provides a unique opportunity to delve into the influence of TiB_2 on corrosion resistance. Notably, Ti+5Ni+5TiB_2 stands out in this regard, boasting the lowest E_{corr} value at –19.00 mV/Ag/AgCl and a relatively modest i_{corr} of 50.40 nA cm^{-2} among the materials involved in the study. These observations strongly indicate that the introduction of TiB_2 nanoparticles engenders a significant enhancement of corrosion resistance. Ti+5Ni+5TiB_2 emerges as a highly promising material, particularly well-suited for applications demanding strong protection against corrosion. The composite materials, Ti+5Ni+15TiB_2 and Ti+5Ni+20TiB_2, present distinct corrosion characteristics. Ti+5Ni+15TiB_2 exhibits an exceptionally elevated i_{corr} value of 783.00 nA cm^{-2}, signaling the presence of severe corrosion. Conversely, Ti+5Ni+20TiB_2 displays a reduced E_{corr} (–53.40 mV/Ag/AgCl) and a lower i_{corr} (33.90 nA cm^{-2}), indicating enhanced resistance to corrosion when compared to Ti+5Ni+15TiB_2. However, it is important to note that the Ti+5Ni+20TiB_2 sample shows wider Tafel

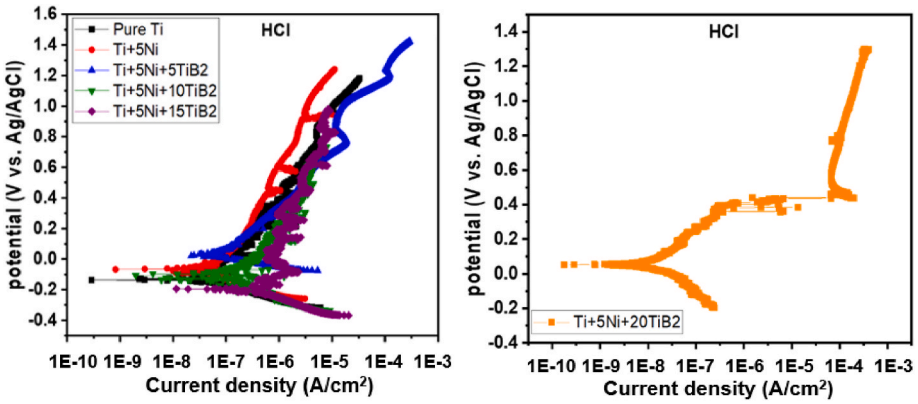

Fig. 4. Potentiodynamic polarization plot of titanium matrix composite in 1 M HCl solution.

Table 4
Electrochemical corrosion parameters of sintered Ti and Ti–Ni-xTiB$_2$ samples following immersion in a 1 M HCl solution.

Sample	$-E_{corr}$ (mV/Ag/AgCl)	i_{corr}(nA cm^{-2})	$-\beta_c$(mV dec^{-1})	β_a(mV dec^{-1})	CR_i(mpy) $\times 10^{-3}$
	HCl				
Pure Ti	135.00	57.30	107.80	451.60	26.58
Ti+5Ni	83.90	42.20	98.90	328.90	19.58
Ti+5Ni+5TiB2	19.00	50.40	65.10	316.70	23.39
Ti+5Ni+10TiB2	123.39	88.00	98.70	224.20	40.84
Ti+5Ni+15TiB2	196.00	783.00	158.60	2.56	363.60
Ti+5Ni+20TiB2	53.40	33.90	253.10	556.90	15.75

slopes (β_c and β_a), implying the potential presence of more intricate corrosion kinetics.

The Ti+5Ni+20TiB$_2$ sample shows a broader active passivation behavior, in comparison to the remaining samples. However, the Ti+5Ni+20TiB$_2$ composite exhibits the lowest corrosion current density and corrosion rate (15.75 x 10^{-3} mpy) compared to the other samples. This observation indicates that among all the samples, the Ti+5Ni+20TiB$_2$ composite demonstrates the most stable passive film, the lowest corrosion rate, and exceptional corrosion resistance. Also, all the titanium matrix samples exhibit a more negative E_{corr}, as shown in Table 4. This is an additional indication of these material's thermodynamic instability when exposed to a highly corrosive environment with an elevated corrosion rate [51]. Considering these corrosion parameters, as shown in Table 4, the corrosion resistance of the six materials follows a descending order as follows: Ti+5Ni+20TiB$_2$ > Ti+5Ni > Ti+5Ni+5TiB$_2$ > Ti > Ti+5Ni+10TiB$_2$ > Ti+5Ni+15TiB$_2$.

3.5. Electrochemical impedance spectroscopy of the composites

The electrochemical impedance spectroscopy (EIS) technique was employed to evaluate the corrosion protection performance of the specimens. This method measures various parameters including the resistance of the electrolyte (R_s), the resistance of the charge transfer process (R_{ct}), and the constant phase element (CPE). Fig. 5 depicts the results of the EIS measurement, presenting both the Nyquist plot and Bode phase plots of the impedance spectra following passivation in a 3.5 wt% NaCl solution. Table 5 also presents the EIS data obtained from the Ti and Ti–Ni-xTiB samples in a 3.5 wt% NaCl solution. Fig. 5(a–b) illustrates that the titanium matrix composite samples revealed a slightly larger semi-circle diameter, in comparison to the 15TiB$_2$ and 20TiB$_2$ samples. The Bode plots show that as the reinforcement in the titanium matrix increases, the impedance modulus experiences a slight rise at lower frequencies, as depicted in Fig. 5(c). As indicated by the Bode diagram, in the low and mid-frequency range, both materials displayed phase angle values close to −90°. This phenomenon indicates the distinctive capacitive behavior attributed to the formation of a highly stable film on the composite in the utilized electrolyte [52]. Higher impedance indicates greater resistance to the electrochemical processes that cause corrosion. This makes it more difficult for corrosion reactions to occur. However, at higher frequencies, the composites with Ti+5Ni+5TiB$_2$, especially Ti+5Ni+20TiB$_2$, have a higher impedance modulus than Ti+5Ni+5TiB$_2$ and the other titanium matrix composites. Li et al. [53] found that higher impedance and electrochemical transfer resistance lead to better corrosion resistance.

The EIS dataset was fitted using the equivalent circuit given in Fig. 5 (e). In the equivalent circuit, R_s represents the solution resistance, R_{ct} denotes the charge transfer resistance, and W is the Warburg diffusion coefficient. The constant phase element (∅) which was needed due to the imperfection of the capacitive loop has two components. These are the ∅ constant (Y_0) and the phase shift indicator (n). They are related following Eq. (3) [54,55]:

$$Z_{CPE} = \frac{1}{Y_0(j\omega)^n} \tag{3}$$

where $j = \sqrt{-1}$ and ω is the angular frequency. The Y_0 behaves as a typical capacitor when the value of n approaches 1. Both n and Y_0 values can be used to qualify a corroding surface and the quality of the corrosion products. Normally, a small value of Y_0 implies a good surface film quality [55]. The quantitative results are summarized in Table 5. R_s denotes the resistance originating from the electrolyte solution employed during EIS measurements, and it is a crucial factor for impedance analysis. Within this dataset, the R_s values span a range from 2.71 to 3.76 Ω cm^2 among different samples, with the lowest R_s observed in pure Ti (2.71 Ω cm^2) and the highest in Ti+5Ni+15TiB$_2$ (3.76 Ω cm^2). These values elucidate the resistance inherent to the experimental electrolyte solutions and offer insights into the conductive properties of each sample's solution. Generally, lower R_s values indicate superior electrolyte conductivity, whereas higher values imply increased resistance to ion flow within the solution. The incorporation of reinforcement into pure titanium initially results in a reduction in the R_s value. However, as the level of reinforcement is further increased, the R_s value surpasses that of Pure titanium and stabilizes. It maintains a similar level, as the electrolyte remains consistent across all samples.

The expansion of the capacitive loop is a direct result of the rise in the R_{ct} (charge transfer resistance) value. R_{ct} values exhibit substantial variations, ranging from 29.06 to 5095.00 Ω cm^2 for different samples. Notably, pure Ti displays the lowest R_{ct} value (29.06 Ω cm^2), indicating relatively efficient charge transfer kinetics. Conversely, Ti+5Ni+5TiB$_2$ stands out with an exceptionally high R_{ct} (5095.00 Ω cm^2), suggesting considerably slower charge transfer kinetics in this specific sample. The CPE index (n) values for all samples are approximately 1, signifying that the surface passivation layers in the titanium matrix composite exhibit

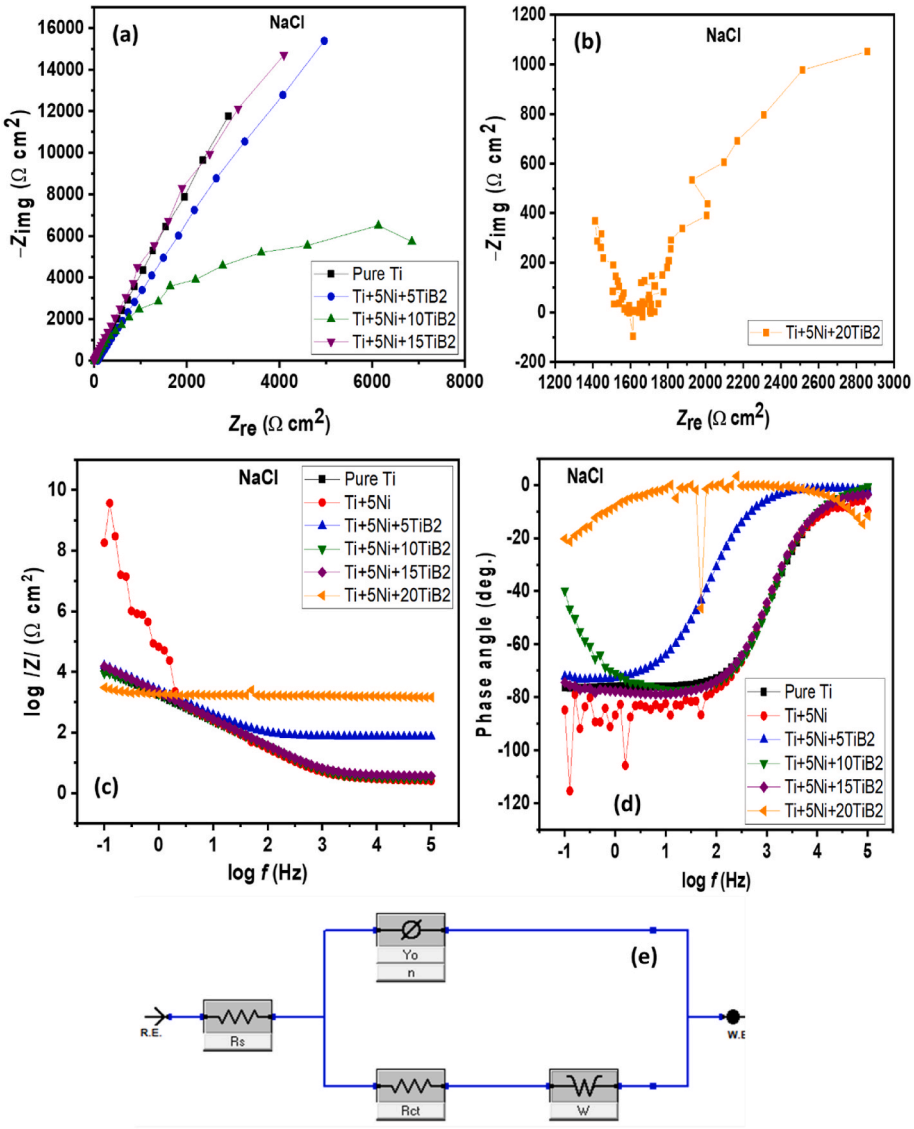

Fig. 5. EIS spectra diagrams, (a,b) Nyquist plot, (c–d) bode plots, (e) equivalent circuit used for impedance analysis.

Table 5
Results from fitting the Electrochemical Impedance Spectroscopy (EIS) data obtained from Ti and Ti–Ni-xTiB$_2$ samples, which were fabricated using spark plasma sintering and immersed in a NaCl solution at room temperature.

Sample	R_s (Ω cm^2)	CPE		R_{ct} (Ω cm^2)	W ($\times \times 10^{-6}$)	x^2 ($\times 10^{-3}$)
		Y_0 ($\mu\Omega^{-1}$ s^2 cm^{-2})	n			
Pure Ti	3.18	118.20	0.86	29.06	5.86	0.25
Ti+5Ni	2.71	111.20	0.90	80.97	−73.10	21.48
Ti+5Ni+5TiB2	2.76	86.34	0.84	5095.00	5.45	0.09
Ti+5Ni+10TiB2	3.14	67.61	0.94	61.82	89.40	6.20
Ti+5Ni+15TiB2	3.76	89.65	0.89	42.24	9.49	0.45
Ti+5Ni+20TiB2	3.62	7.18	0.77	1557.00	992.00	1.67

purely capacitive behavior, regardless of the TiB$_2$ content [56].

Fig. 6 shows the EIS results for the sintered titanium matrix composite in a 1 M HCl solution. These are presented in the form of Nyquist diagrams and Bode plots. Table 6 displays the EIS data obtained from Ti and Ti–Ni-xTiB samples in a 1 M HCl solution. The equivalent circuit in Fig. 5(e) was used for all the analyses, except for the Ti+5Ni+20TiB$_2$ data where the equivalent circuit shown in Fig. 6(e) was used. Relative to Fig. 6(a), a clear oxide layer contribution depicted by a well-formed capacitive loop at high-to-medium frequencies is observed in Fig. 6(b). Hence, the equivalent circuit in Fig. 6(e) with an element R_o that accounts for the resistance of the oxide layer was used in fitting the Ti+5Ni+20TiB$_2$ data. A critical parameter in the EIS analysis is R_s, or sheet resistance, which provides insights into how easily a material conducts electrical current across its surface. Lower R_s values indicate superior conductivity, allowing electrons to move more freely through the material. Conversely, higher R_s values signify increased resistance,

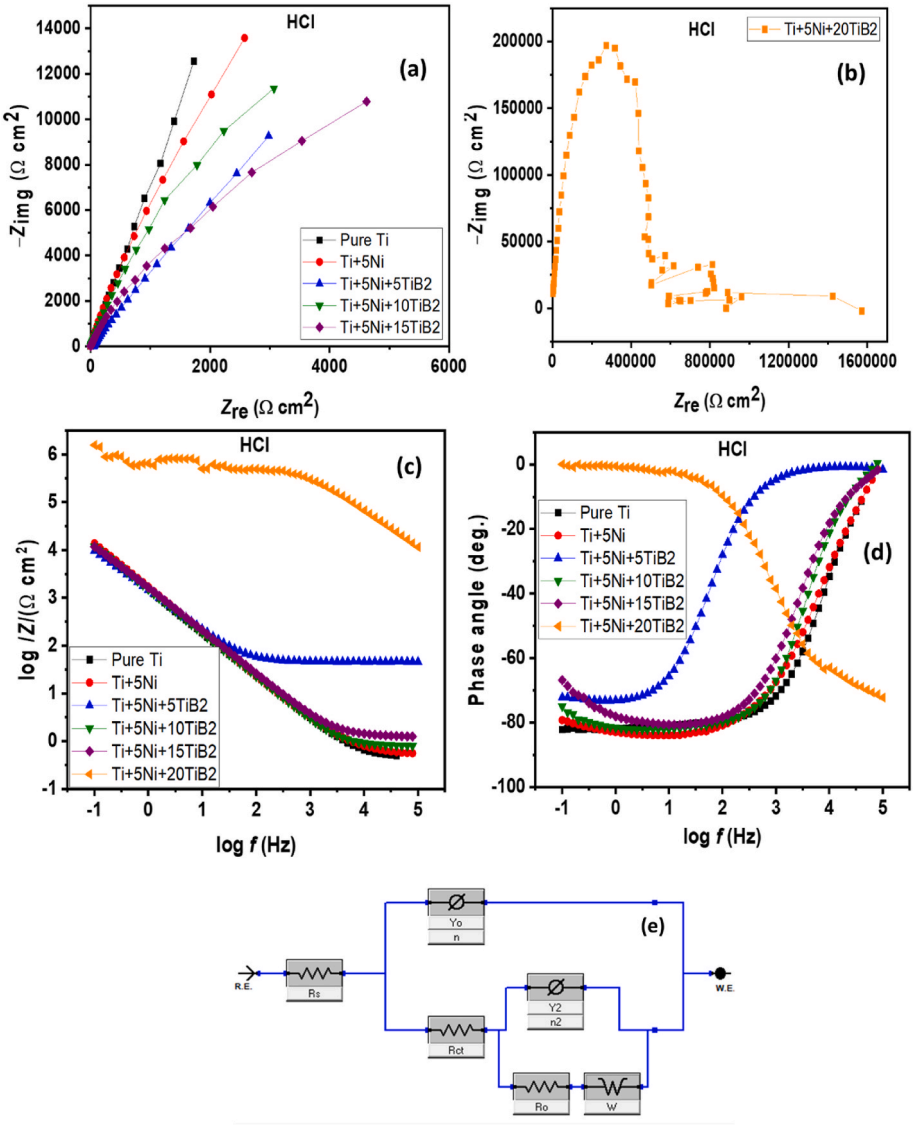

Fig. 6. EIS spectra diagrams, (a,b) Nyquist plot, (c–d) bode plots, (e) equivalent circuit used for impedance analysis.

Table 6
Results from fitting the Electrochemical Impedance Spectroscopy (EIS) data obtained from Ti and Ti–Ni-xTiB samples, which were fabricated using spark plasma sintering and immersed in an HCl solution at room temperature.

Sample	R_s(Ω cm^2)	CPE		R_{ct}(Ω cm^2)	W(× 10^{-6})	x^2 (× 10^{-3})	R_o(Ω cm^2)	CPE_o	
		Y_0(μΩ^{-1} s^2 cm^{-2})	n					Y_2(μΩ^{-1} s^2 cm^{-2})	n_2
	HCl								
Pure Ti	0.48	133.00	0.90	569.10	−9.98	0.17	–	–	–
Ti+5Ni	0.60	117.00	0.91	1256.00	−5.80	3.60	–	–	–
Ti+5Ni+5TiB2	0.46	131.00	0.87	4576.00	26.54	0.05	–	–	–
Ti+5Ni+10TiB2	0.81	118.50	0.92	101.50	11.99	0.52	–	–	–
Ti+5Ni+15TiB2	1.30	103.30	0.91	15.58	30.60	1.23	–	–	–
Ti+5Ni+20TiB2	0.16	114.40	1.00	543300.00	35.24	21.60	184000.00	20.80	0.80

resulting in decreased conductivity. In Fig. 6, the R_s values vary from 0.16 Ω cm^2 for Ti+5Ni+20TiB$_2$ to 1.30 Ω cm^2 for Ti+5Ni+15TiB$_2$. The remarkably low R_s for Ti+5Ni+20TiB$_2$ suggests efficient ionic transport in the HCl solution, potentially enhancing its electrochemical performance. The CPE index (n) values for all samples are approximately 1, suggesting that the surface passivation layers in the titanium matrix composite display purely capacitive behavior, regardless of the TiB$_2$ content [56].

R_{ct} represents another vital impedance parameter that signifies the resistance to charge transfer occurring at the interface between the electrode and the electrolyte. A low R_{ct} indicates efficient electron transfer. Contrastingly, a high R_{ct} suggests poor electron transfer, which can hinder electrochemical reactions. Using polarization curves in Nyquist plots, the charge transfer resistance (R_{ct}) of Ti+5Ni+20TiB$_2$ is observed to reach its maximum value at 543,300.00 Ω cm^2, indicating slower charge transfer kinetics. This elevated R_{ct} value may suggest that

Ti+5Ni+20TiB_2 offers better corrosion resistance, as slower charge transfer can lead to reduced corrosion rates. Moreover, the impedance analysis characterizes the diffusion behavior of ions or species within the passive layer. High impedance values signify efficient diffusion, while lower values suggest slower diffusion rates. The Bode plots in Fig. 6(c) illustrate that with an increase in the reinforcement content within the titanium matrix, the impedance modulus experiences a slight upturn at lower frequencies. As demonstrated by the Bode diagram, within the low and middle-frequency range, both materials exhibit phase angle values approaching −90°. This behavior signifies the distinct capacitive characteristics resulting from the formation of a highly stable film in the composite electrolyte utilized [57]. Ti+5Ni+20TiB_2 stands out with significantly high impedance values, indicating enhanced diffusion properties within its passive layer. Conversely, Ti+5Ni exhibits lower impedance values, suggesting restricted diffusion within the passive layer.

Furthermore, this distinction implies that Ti+5Ni+20TiB_2 may possess a passive layer that is more porous and permeable, potentially offering advantages in terms of corrosion resistance. Research conducted by Lavos-Valereto et al. [58], found that the barrier layer is the most important part of the passive layer's efficiency in protecting the metal from corrosion. This is consistent with previous findings indicating that the barrier layer is mainly responsible for the corrosion resistance of the Ti–6Al–7Nb alloy, while the porous layer primarily accounts for the osseointegration (the ability of the metal to bond with bone). Hence, Ti+5Ni+20TiB_2 emerges as a highly promising material for applications demanding corrosion resistance. It is distinguished by its minimal solution resistance, well-maintained passive layer, effective diffusion characteristics, strong capacitive behavior, and a comparatively direct impedance response.

4. Conclusion

In summary, the research investigated the microstructural changes, hardness prediction using response surface methodology, and corrosion performance of titanium matrix composites reinforced with TiB_2 in both 3.5 wt% NaCl and 1 M HCl solutions. The following conclusions can be drawn, based on the results:

1. Incorporating nickel (Ni) and titanium diboride (TiB_2) into the titanium matrix led to significant microstructural changes, resulting in a coexistence of α and β phases along grain boundaries. Ti+5Ni+20TiB_2 exhibited a larger equiaxed α phase.
2. The XRD analysis showed altered crystal structures with broader peaks and shifts in peak positions, indicating finer grains in both α and β phases. This was due to rapid heating and cooling during sintering.
3. The addition of TiB_2 increased microhardness (238–592 $HV_{0.2}$). This was attributed to the ceramic (TiB_2) hardness and its hindrance to dislocation movement. The regression analysis provided insights into the hardness-reinforcement content relationship. The cubic model was highlighted as the preferred choice among the other models. Also, the F-value, as indicated at 6515.76, reinforced the model's significance.
4. In the potentiodynamic polarization test, it was found that the addition of nickel and titanium diboride (TiB_2) improved the corrosion resistance, with Ti+5Ni+20TiB_2 showing the best resistance in both environments. Ti+5Ni+5TiB_2 emerged as a promising material for strong corrosion protection in the HCl solution. Overall, Ti+5Ni+20TiB_2 displayed the most stable passive film and superior corrosion resistance in both test environments.
5. This research has demonstrated that increased reinforcement content in titanium matrix composites improves corrosion resistance in the EIS technique, as demonstrated by higher impedance values in a 3.5 wt% NaCl solution. Variations in solution resistance (R_s) and charge transfer resistance (R_{ct}) indicated enhanced electrolyte conductivity and reduced corrosion rates, particularly in Ti+5Ni+20TiB_2. In 1 M HCl solution, Ti+5Ni+20TiB_2 exhibited efficient electrical conductivity, slower charge transfer kinetics (high R_{ct}), and enhanced diffusion properties within its passive layer. This makes it a promising choice for applications requiring strong corrosion protection.

Declaration of competing interest

The authors declare that they have no known competing financial interests or personal relationships that could have appeared to influence the work reported in this paper.

Acknowledgments

The authors are grateful to the National Research Foundation (NRF) of South Africa and North-West University, South Africa, for funding this study.

References

[1] D. Banerjee, J.C. Williams, Perspectives on titanium science and technology, Acta Mater. 61 (2013) 844–879.
[2] O.E. Falodun, B.A. Obadele, S.R. Oke, O.O. Ige, P.A. Olubambi, Effect of TiN and TiCN additions on spark plasma sintered Ti–6Al–4V, Part. Sci. Technol. 38 (2020), https://doi.org/10.1080/02726351.2018.1515798.
[3] M. Selvakumar, T. Ramkumar, P. Chandrasekar, Thermal characterization of titanium–titanium boride composites, J. Therm. Anal. Calorim. 136 (2019) 419–424.
[4] Y.J. Yang, Z.P. Zhang, Z.S. Jin, W.C. Sun, C.Q. Xia, M.Z. Ma, X.Y. Zhang, G. Li, R. P. Liu, A study on the corrosion behavior of the in-situ Ti-based bulk metallic glass matrix composites in acid solutions, J. Alloys Compd. 782 (2019) 927–935.
[5] C.G. Nava-Dino, C. López-Meléndez, R.G. Bautista-Margulis, M.A. Neri-Flores, J. G. Chacón-Nava, S.D. De la Torre, J.G. Gonzalez-Rodriguez, A. Martínez-Villafañe, Corrosion behavior of Ti-6Al-4V alloys, Int. J. Electrochem. Sci. 7 (2012) 2389–2402.
[6] C. Veiga, J.P. Davim, A.J.R. Loureiro, Properties and applications of titanium alloys: a brief review, Rev. Adv. Mater. Sci. 32 (2012) 133–148.
[7] O.E. Falodun, B.A. Obadele, S.R. Oke, O.O. Ige, P.A. Olubambi, M.L. Lethabane, S. W. Bhero, Influence of spark plasma sintering on microstructure and wear behaviour of Ti-6Al-4V reinforced with nanosized TiN, Trans. Nonferrous Metals Soc. China (2018) 28, https://doi.org/10.1016/S1003-6326(18)64637-0 (English Edition).
[8] B. Dutta, F.H.S. Froes, The additive manufacturing (AM) of titanium alloys, Met. Powder Rep. 72 (2017) 96–106.
[9] F. Romero, V. Amigó, M.D. Salvador, E. Martinez, Mechanical and microstructural properties of titanium matrix composites reinforced by TiN particles, in: Materials Science Forum, Trans Tech Publ, 2007, pp. 825–828.
[10] W.J. Lu, L. Xiao, K. Geng, J.N. Qin, D. Zhang, Growth mechanism of in situ synthesized TiBw in titanium matrix composites prepared by common casting technique, Mater. Char. 59 (2008) 912–919.
[11] Z. Yin, J. Yuan, W. Xu, M. Chen, S. Yan, Z. Wang, Effect of Ni and graphene on microstructure and toughness of titanium boride ceramic tool material prepared by spark plasma sintering, Ceram. Int. 44 (2018) 20299–20305.
[12] X. Yue, Z. Cai, X. Lü, J. Wang, H. Ru, Effect of Ni content on microstructures and mechanical properties of hot-pressed TiC–TiB_2–Ni composite, Materials Science and Engineering: A 668 (2016) 208–214.
[13] M. Gu, C. Huang, B. Zou, B. Liu, Effect of (Ni, Mo) and TiN on the microstructure and mechanical properties of TiB_2 ceramic tool materials, Materials Science and Engineering: A 433 (2006) 39–44.
[14] O.E. Falodun, S.R. Oke, P.A. Olubambi, J.O. Dirisu, R. Sule, Microstructural characteristics and wear behavior of sintered Ni-modified Ti–x TiB_2 composites, J. Inst. Eng. (2023) 1–10. Series D.
[15] O.M. Ivasishin, D.G. Sawakin, V.S. Moxson, K.A. Bondareval, F.H. Froes, Titanium powder metallurgy for automotive components, Mater. Technol. 17 (2002) 20–25.
[16] K. Kondoh, Titanium metal matrix composites by powder metallurgy (PM) routes, in: Titanium Powder Metallurgy, Elsevier, 2015, pp. 277–297.
[17] O.E. Falodun, B.A. Obadele, S.R. Oke, A.M. Okoro, P.A. Olubambi, Titanium-based matrix composites reinforced with particulate, microstructure, and mechanical properties using spark plasma sintering technique: a review, Int. J. Adv. Manuf. Technol. 102 (2019), https://doi.org/10.1007/s00170-018-03281-x.
[18] A.M. Okoro, R. Machaka, S.S. Lephuthing, S.R. Oke, M.A. Awotunde, P. A. Olubambi, Evaluation of the sinterability, densification behaviour and microhardness of spark plasma sintered multiwall carbon nanotubes reinforced Ti6Al4V nanocomposites, Ceram. Int. 45 (2019) 19864–19878.
[19] O.O. Ayodele, B.J. Babalola, P.A. Olubambi, Microstructures and mechanical properties of ceramics reinforced titanium matrix fabricated by pulsed electric current sintering, J. Mater. Res. Technol. 17 (2022) 2807–2817.
[20] S.O. Akinwamide, M. Maleka, N. Motabeni, O.J. Akinribide, F.E. Oluwasegun, P. A. Olubambi, Synthesis and characterization of spark plasma sintered zirconia and

ferrotitanium reinforced hybrid aluminium composite, Int. J. Adv. Des. Manuf. Technol. 125 (2023) 763–776.
[21] N. Zhang, X. Han, D. Sun, S. Liu, H. Liu, W. Yang, G. Wu, Microstructure evolution and mechanical properties of LaB6-modified Ti2AlNb alloy fabricated by blended elemental powder metallurgy, Powder Technol. 369 (2020) 334–344.
[22] A. Sergi, R.H.U. Khan, S. Irukuvarghula, M. Meisnar, A. Makaya, M.M. Attallah, Development of Ni-base metal matrix composites by powder metallurgy hot isostatic pressing for space applications, Adv. Powder Technol. 33 (2022) 103411.
[23] M.S. Kumar, P. Chandrasekar, P. Chandramohan, M. Mohanraj, Characterisation of titanium–titanium boride composites processed by powder metallurgy techniques, Mater. Char. 73 (2012) 43–51.
[24] O.E. Falodun, B.A. Obadele, S.R. Oke, A.M. Okoro, P.A. Olubambi, Titanium-based matrix composites reinforced with particulate, microstructure, and mechanical properties using spark plasma sintering technique: a review, Int. J. Adv. Des. Manuf. Technol. 102 (2019) 1689–1701.
[25] S.C. Tjong, Y.-W. Mai, Processing-structure-property aspects of particulate-and whisker-reinforced titanium matrix composites, Compos. Sci. Technol. 68 (2008) 583–601.
[26] L.L. Dong, B. Xiao, Y. Liu, Y.L. Li, Y.Q. Fu, Y.Q. Zhao, Y.S. Zhang, Sintering effect on microstructural evolution and mechanical properties of spark plasma sintered Ti matrix composites reinforced by reduced graphene oxides, Ceram. Int. 44 (2018) 17835–17844.
[27] A. Sabahi Namini, M. Azadbeh, Microstructural characterisation and mechanical properties of spark plasma-sintered TiB_2-reinforced titanium matrix composite, Powder Metall. 60 (2017) 22–32.
[28] I. Sulima, R. Kowalik, P. Hyjek, The corrosion and mechanical properties of spark plasma sintered composites reinforced with titanium diboride, J. Alloys Compd. 688 (2016) 1195–1205.
[29] N. Abu-Warda, M.D. Lopez, M.D. Escalera-Rodríguez, E. Otero, M. V Utrilla, Corrosion behavior of mechanically alloyed A6005 aluminum alloy composite reinforced with TiB2 nanoparticles, Mater. Corros. 71 (2020) 382–391.
[30] S.-H. Chang, C.-H. Liang, K.-T. Huang, C. Liang, Evaluation of the microstructures, strengthening mechanisms and corrosion behaviors of TiB_2 powder added to Ti–8Ta–6Ni alloys through the vacuum sintering process, J. Alloys Compd. 857 (2021) 157629.
[31] S.S. Sahay, K.S. Ravichandran, R. Atri, B. Chen, J. Rubin, Evolution of microstructure and phases in in situ processed Ti–TiB composites containing high volume fractions of TiB whiskers, J. Mater. Res. 14 (1999) 4214–4223.
[32] A. Sabahi Namini, M. Azadbeh, M. Shahedi Asl, Effects of in-situ formed TiB whiskers on microstructure and mechanical properties of spark plasma sintered Ti–B4C and Ti–TiB2 composites, Sci. Iran. 25 (2018) 762–771.
[33] C. Suryanarayana, N. Al-Aqeeli, Mechanically alloyed nanocomposites, Prog. Mater. Sci. 58 (2013) 383–502.
[34] B.S. Murty, S. Ranganathan, Novel materials synthesis by mechanical alloying/milling, Int. Mater. Rev. 43 (1998) 101–141.
[35] A. Couret, G. Molénat, J. Galy, M. Thomas, Microstructures and mechanical properties of TiAl alloys consolidated by spark plasma sintering, Intermetallics 16 (2008) 1134–1141.
[36] B.A. Obadele, O.E. Falodun, S.R. Oke, P.A. Olubambi, Spark Plasma Sintering Behaviour of Commercially Pure Titanium Micro-alloyed with Ta-Ru, Particulate Science and Technology, 2018.
[37] Y. Wang, M. Zhu, L. Dong, G. Sun, W. Zhang, H. Xue, Y. Fu, A. Elmarakbi, Y. Zhang, In-situ synthesized TiC/Ti-6Al-4V composites by elemental powder mixing and spark plasma sintering: microstructural evolution and mechanical properties, J. Alloys Compd. (2023) 169557.
[38] Y. Xiong, F. Zhang, Y. Huang, C. Shang, Q. Wan, Multiple strengthening via high-entropy alloy particle addition in titanium matrix composites fabricated by spark plasma sintering, Materials Science and Engineering: A 859 (2022) 144235.
[39] P. Nandwana, J.Y. Hwang, M.Y. Koo, J. Tiley, S.H. Hong, R. Banerjee, Formation of equiaxed alpha and titanium nitride precipitates in spark plasma sintered TiB/Ti–6Al–4V composites, Mater. Lett. 83 (2012) 202–205.
[40] H.A.N. Chao, Y. Li, X. Liang, L. Chen, Z. Na, X. Zhu, Effect of composition and sintering temperature on mechanical properties of ZrO_2 particulate-reinforced titanium-matrix composite, Trans. Nonferrous Metals Soc. China 22 (2012) 1855–1859.
[41] S.O. Akinwamide, S. Bossuyt, E.A.K. Fangnon, O.J. Akinribide, P.A. Olubambi, Characterization of pulse electric current sintered Ti-6Al-4V ternary composites: role of YSZ-Si3N4 ceramics addition on structural modification and hydrogen desorption, Mater. Today Commun. 36 (2023) 106706.
[42] O.E. Falodun, B.A. Obadele, S.R. Oke, M.E. Maja, P.A. Olubambi, Synthesis of Ti-6Al-4V alloy with nano-TiN microstructure via spark plasma sintering technique, IOP Conf. Ser. Mater. Sci. Eng. (2017), https://doi.org/10.1088/1757-899X/272/1/012029.
[43] X. Nie, H. Zhang, H. Zhu, Z. Hu, L. Ke, X. Zeng, Analysis of processing parameters and characteristics of selective laser melted high strength Al-Cu-Mg alloys: from single tracks to cubic samples, J. Mater. Process. Technol. 256 (2018) 69–77.
[44] S. Pan, J. Yuan, C. Linsley, J. Liu, X. Li, Corrosion behavior of nano-treated AA7075 alloy with TiC and TiB2 nanoparticles, Corros Sci 206 (2022) 110479.
[45] Y. Chen, J. Zhang, N. Dai, P. Qin, H. Attar, L.-C. Zhang, Corrosion behaviour of selective laser melted Ti-TiB biocomposite in simulated body fluid, Electrochim. Acta 232 (2017) 89–97.
[46] Y. Guo, X. Shang, Q. Liu, Microstructure and properties of in-situ TiN reinforced laser cladding $CoCr_2FeNiTix$ high-entropy alloy composite coatings, Surf. Coat. Technol. 344 (2018) 353–358.
[47] N. Dai, L.-C. Zhang, J. Zhang, X. Zhang, Q. Ni, Y. Chen, M. Wu, C. Yang, Distinction in corrosion resistance of selective laser melted Ti-6Al-4V alloy on different planes, Corros Sci 111 (2016) 703–710.
[48] Y. Wang, Z. Xu, A. Zhang, Electrochemical dissolution behavior of Ti-45Al-2Mn-2Nb+ 0.8 vol% TiB2 XD alloy in NaCl and $NaNO_3$ solutions, Corros Sci 157 (2019) 357–369.
[49] B. Wu, Z. Pan, S. Li, D. Cuiuri, D. Ding, H. Li, The anisotropic corrosion behaviour of wire arc additive manufactured Ti-6Al-4V alloy in 3.5% NaCl solution, Corros Sci 137 (2018) 176–183.
[50] X. Cheng, Y. Huang, B. Zhou, P. Xue, H. Fan, J. Sun, Electrochemical and XPS studies of a Nb-containing Ti-based glass-forming alloy system in H_2SO_4 solution, Electrochem. Commun. 60 (2015) 139–143.
[51] X. Wang, L. Zhang, X. Zhou, W. Wu, X. Jie, Corrosion behavior of Al_2O_3-reinforced graphene encapsulated Al composite coating fabricated by low pressure cold spraying, Surf. Coat. Technol. 386 (2020) 125486.
[52] S.L. de Assis, S. Wolynec, I. Costa, Corrosion characterization of titanium alloys by electrochemical techniques, Electrochim. Acta 51 (2006) 1815–1819.
[53] Q. Li, S.S. Liu, X.H. Wang, T. Yang, C. Dong, J.T. Hu, Y.Q. Jiang, Mechanical and corrosion properties of Ti-Ni-Cu-Zr metallic glass matrix composites, J. Alloys Compd. 727 (2017) 1344–1350.
[54] Y. Jiang, Y. Liu, S. Gao, X. Guo, J. Zhang, Experimental and theoretical studies on corrosion inhibition behavior of three imidazolium-based ionic liquids for magnesium alloys in sodium chloride solution, J. Mol. Liq. 345 (2022) 116998.
[55] H. Gerengi, N. Sen, I. Uygur, M.M. Solomon, Corrosion response of ultra-high strength steels used for automotive applications, Mater. Res. Express 6 (2019) 0865a6.
[56] X. Meng, J. Guan, Q. Liu, P. Liang, Y. Wang, Investigation on the microstructure and electrochemical corrosion properties of TiB_2 reinforced aluminum matrix composites, Int. J. Electrochem. Sci. 17 (2022) 220640.
[57] J.E.G. Gonzalez, J.C. Mirza-Rosca, Study of the corrosion behavior of titanium and some of its alloys for biomedical and dental implant applications, J. Electroanal. Chem. 471 (1999) 109–115.
[58] I.C. Lavos-Valereto, S. Wolynec, I. Ramires, A.C. Guastaldi, I. Costa, Electrochemical impedance spectroscopy characterization of passive film formed on implant Ti–6Al–7Nb alloy in Hank's solution, J. Mater. Sci. Mater. Med. 15 (2004) 55–59.